



Dynamic rupture of subduction earthquakes located near the trench

Cristian Otarola^{a,*}, Sergio Ruiz^a, Carlos Herrera^b, Raúl Madariaga^c, Cristián Siegel^a

^a Departamento de Geofísica, Facultad de Ciencias Físicas y Matemáticas, Universidad de Chile, Blanco Encalada 2002, Santiago, Chile

^b School of Earth and Ocean Sciences, University of Victoria, 3800 Finnerty Road Victoria, British Columbia V8P 5C2, Canada

^c Département de Géologie, Ecole Normale Supérieure, PSL University, 75005 Paris, France

ARTICLE INFO

Article history:

Received 28 May 2020

Received in revised form 1 February 2021

Accepted 16 February 2021

Available online xxxx

Editor: J.-P. Avouac

Keywords:

source seismic

dynamic inversion

dynamic source parameters

subduction earthquakes

ABSTRACT

We perform kinematic and dynamic source inversions of four interplate thrust earthquakes that occurred near the trench at the base of the continental wedge in Northern Chile and we compare them to deeper intraplate events. The magnitudes of these interplate events were between Mw 6.3 and Mw 6.5, with hypocentral depths varying between 17.8 km and 28 km. These earthquakes correspond to one foreshock and three aftershocks of the large 2014 Mw 8.2 Iquique earthquake. The geometry of the seismic rupture obtained from the kinematic and dynamic inversions were similar for the four earthquakes studied and their dynamic source parameters are in accordance with typical interplate earthquakes around Mw 6.5. We compare the dynamic rupture of these events with those of five intraplate, intermediate-depth earthquakes that occurred in Northern Chile, Japan, Argentina and Mexico with depths between 57 km and 250 km. We also compare these events with the Mw 6.9 Valparaíso earthquake that was also a shallow interplate thrust event. Results show that the main dynamic parameters of the interplate events (stress in the nucleation zone, overall stress drop and fracture energy rate) were smaller than those of the intraplate intermediate-depth earthquakes. Furthermore, we compare our results with those obtained with several methodologies commonly used to estimate values of stress drop, fault radius and corner frequency. We find some minor differences between them for most of the earthquakes analyzed. Finally, we infer from our results that the studied area, located in the subduction interface zone near the trench, is suitable for earthquake nucleation of small to moderate earthquakes and does not represent a barrier for a future large tsunamigenic rupture.

© 2021 Elsevier B.V. All rights reserved.

1. Introduction

Dynamic models of the earthquake source take into consideration stress-strain states and the friction laws governing the rupture of earthquakes. The slip on the fault is considered as a consequence of the stress conditions and the strength of the material in the focal region. The dynamic characteristics of the plate interface contact near the trench have always been of interest to the scientific community.

Northern Chile is an active seismic zone where large tsunamigenic earthquakes have occurred in the past (Ruiz and Madariaga, 2018). In this work, we use four events with magnitudes between Mw 6.3 and Mw 6.5 to study the friction properties on the plate interface in this region. These events were one foreshock and three aftershocks of the Mw 8.2 earthquake that occurred offshore of the city of Iquique on April 1st, 2014 (see Fig. 1). The mainshock rupture occurred on the plate interface and did not reach the trench

(Lay et al., 2014; Ruiz et al., 2014; Schurr et al., 2014; Duputel et al., 2015), whereas the foreshocks and aftershocks were located closer to the trench under the continental wedge (Fig. 1). The 2014 Iquique main-shock was preceded by an intense foreshock activity and most probably by a slow slip event (Ruiz et al., 2014; Kato et al., 2016; Socquet et al., 2017). The largest foreshock (Mw 6.7) was located inside the upper plate and it was associated to the activation of a landward-verging normal structure of high-angle (González et al., 2015; Maksymowicz et al., 2018; Ruiz et al., 2019). The largest aftershock of the Iquique earthquake occurred in a deeper section of the plate interface with a magnitude Mw 7.7 and several events with magnitudes around Mw 6.5 were reported close to the main-shock rupture area. Most of the foreshocks and aftershocks were interplate thrust events (León-Ríos et al., 2016; Cesca et al., 2016; Soto et al., 2019), Fig. 1.

The fore arc structure of Northern Chile has been studied by various authors (Contreras-Reyes et al., 2012; Geersen et al., 2018; Maksymowicz et al., 2018). In particular, Maksymowicz et al. (2018) proposed three main units in the continental wedge: (1) A frontal accretionary prism (FAP) located in the closest section to

* Corresponding author.

E-mail address: crotarola@ug.uchile.cl (C. Otarola).

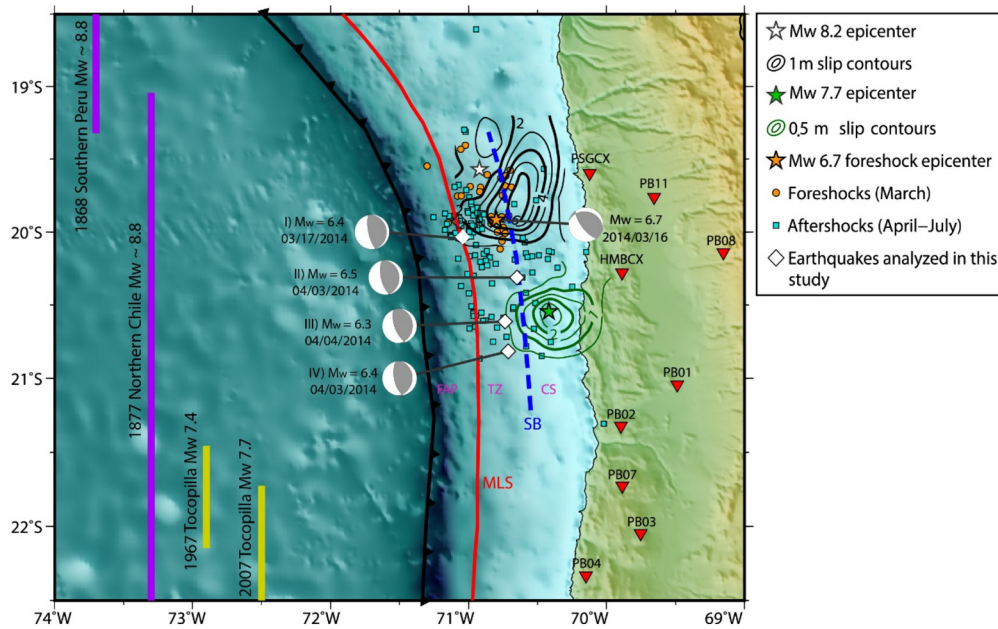


Fig. 1. Seismotectonic context of the Northern Chile and Southern Peru subduction zone. The purple lines are the estimated rupture extent of giant earthquakes and the yellow lines are the rupture lengths of smaller events that broke the interplate contact (Ruiz and Madariaga, 2018). Locations of the $M > 4.0$ foreshocks and aftershocks were obtained by León-Ríos et al. (2016). Co-seismic slip contours of the Mw 8.2 mainshock and its Mw 7.7 aftershock were obtained from kinematic modeling by Ruiz et al. (2014). Global Centroid Moment Tensor focal mechanisms, dates and magnitudes from the United States Geological Survey (USGS) are shown for the four events analyzed in this study and the Mw 6.7 foreshock. The red triangles show the locations of the stations used in the inversion. The red line indicates the limit between the lower and middle slopes (MLS) and the dotted blue line corresponds to the shelf-break (SB), which allow to identify the main units of the continental wedge proposed by Maksymowicz et al. (2018), they are: (1) frontal accretionary prism (FAP), (2) transition zone (TZ) and (3) dense basement below the continental shelf (CS). (For interpretation of the colors in the figure(s), the reader is referred to the web version of this article.)

the trench, which is formed by low density material made of debris with a highly fractured rock, (2) a transition zone (TZ), where the fracturing degree and porosity decreases landwards, correlated with the middle continental slope, and (3) a dense basement below the continental shelf (CS).

As shown in Fig. 1, most of the foreshocks and aftershocks of the 2014 Mw 8.2 Iquique earthquake are located approximately in the TZ, where the four interplate events studied in this work occurred. In total, three foreshocks and four aftershocks of magnitude $M_w > 6.0$ occurred in the TZ, but from those, only four events with magnitudes between $M_w 6.3$ and $M_w 6.5$ (the largest ones) were well recorded by strong motion instruments of the Integrated Plate boundary Observatory Chile (IPOC) network and the Centro Sismológico Nacional (CSN) of the Universidad de Chile. We could not study other large-magnitude events, because their body waves overlapped with surface waves of other earthquakes that were part of the very frequent seismicity that occurred during the 2014 Iquique sequence (Ruiz et al., 2014).

In this paper we perform kinematic and dynamic source inversions of these four interplate earthquakes. We consider a simple dynamic approach based on an elliptical fault approximation to simulate the earthquake rupture (Madariaga and Ruiz, 2016). We generate synthetic strong motion records to model the observed strong motion data recorded by a local seismic network (see Fig. 1). We finally compare our results with the dynamic models of five intraplate intermediate depth earthquakes (Ruiz and Madariaga, 2011, 2013; Herrera et al., 2017; Díaz-Mojica et al., 2014; Mirwald et al., 2019) and one interplate thrust earthquake (Ruiz et al., 2017). All of these events were modeled using a similar elliptical shape dynamic inversion method. We determine the dynamic characteristic of the earthquakes that broke the plate interface close to the trench, and study the similarities or differences of their dynamic behavior with other interplate and intraplate earthquakes. Finally, the results of some commonly used methods to

estimate stress drop, fault radius and corner frequency, were compared to the results of our dynamic models.

2. Data and methods

We perform kinematic and dynamic source inversions of the following earthquakes:

- I) March 17th, 2014 at 05:11:34 UTC time, $M_w 6.4$ foreshock;
- II) April 3rd, 2014 at 01:58:30 UTC time, $M_w 6.5$ aftershock;
- III) April 3rd, 2014 at 05:26:15 UTC time, $M_w 6.4$ aftershock;
- IV) April 4th, 2014 at 01:37:50 UTC time, $M_w 6.3$ aftershock.

We previously relocated the hypocenter of these 4 events using the NonLinLoc program (Lomax et al., 2000) with the 1-D velocity model proposed by Husen et al. (1999), see Fig. A.1. In addition, we considered the focal mechanisms reported by the Global Centroid Moment Tensor (GCMT) agency (see Table A.1 and Fig. 1). These events were well recorded by the strong motion instruments of the CSN and IPOC networks (Fig. 1), which are mostly deployed on hard rock (Leyton et al., 2018a, 2018b).

To choose the band-pass filter we consider that the corner frequency of the events is contained in the frequency range of the inversions. To estimate the corner frequency values, we analyzed the strong motion data of five stations with a high signal/noise ratio. The time series were corrected for instrument response, their linear trend was removed and they were integrated twice to obtain displacement time series. Then we computed the Fourier amplitude spectrum (FAS) on the S wave window (Fig. A.2) and fitted Brune's (1970) spectral model (Eq. A.1) over the FAS. We found corner frequencies of 0.18, 0.17, 0.18 and 0.18 Hz for the four events I-IV respectively (Fig. A.3-4). For events II-IV the complete strong motion time series were filtered using a causal band pass Butterworth filter in the range 0.02 Hz to 0.20 Hz. Unfortunately, for event I we could not reach the highest frequency cutoff. The

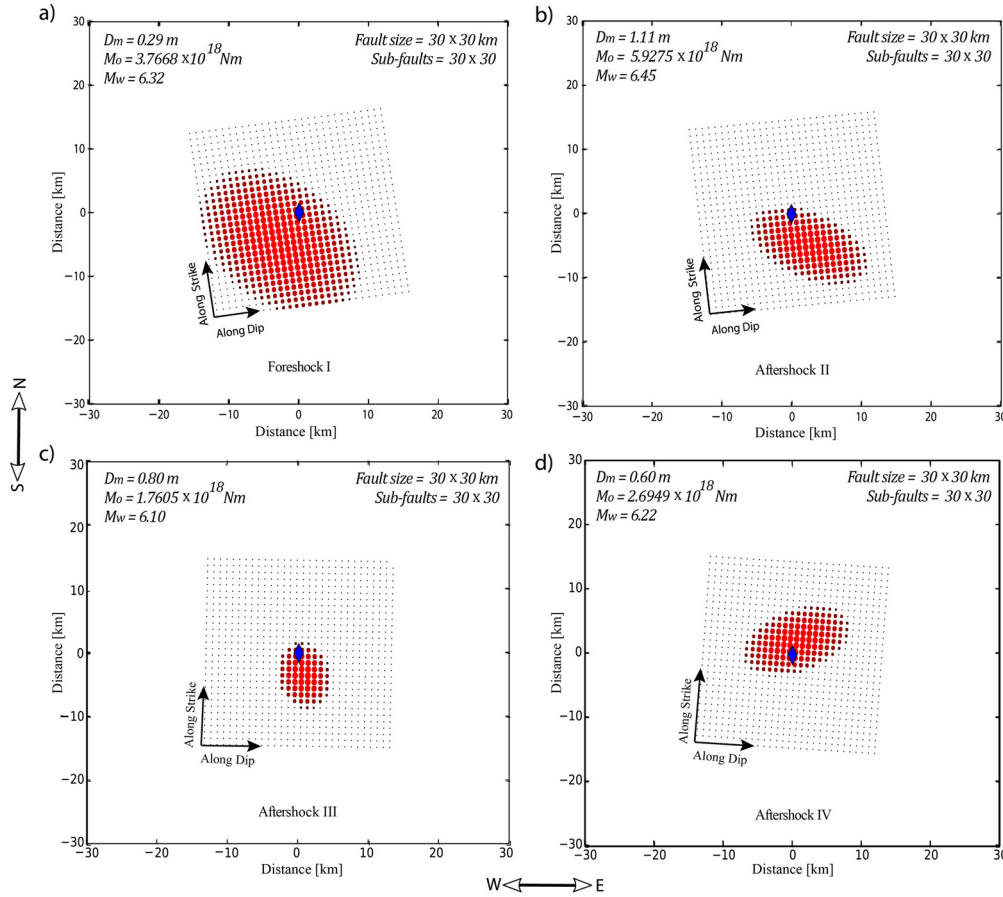


Fig. 2. Slip distribution from kinematic inversion for the four events. The slip on the fault plane is shown with red dots with size proportional to slip. The maximum slip, seismic moment and magnitude M_w for the best model are listed at the top left of each slip distribution.

seismograms for event I contained surface waves that cannot be reproduced by our synthetic seismograms, so data for this event was filtered using a causal bandpass Butterworth filter between 0.02 and 0.18 Hz. We also used the location of the GCMT to obtain better results (see Appendix B). Finally, we carried out the inversion using displacement seismograms of 102.4 s long, starting at the earthquake's origin time.

In order to model the seismic source using local records (epicentral distances less than 300 km), we used the elliptical-fault approximation to perform kinematic and dynamic inversion (i.e. Vallée and Bouchon, 2004; Di Carli et al., 2010; Ruiz and Madariaga, 2011, 2013; Ruiz et al., 2019 and explained in detail in Madariaga and Ruiz, 2016). The kinematic model considers seven parameters to invert. Five are used to describe the geometry of the rupture: the semi-axes (a) and (b) of the elliptical patch, its rotation angle (α) and the location of its center (x_0, y_0) with respect to the hypocenter, where x_0 goes along the strike and y_0 goes along the dip in the fault plane. The other two parameters are: the maximum slip (D_m) on the rupture assuming a centered elliptical slip distribution, and the rupture velocity (v_r). The dynamic model considers ten parameters in the inversion. Five of them describe the geometry of the rupture just as for the kinematic model. Two parameters describe a circular nucleation patch inside the ellipse: the radius R with a stress T'_μ acting inside of the nucleation zone, and three frictional parameters T_e, T_μ and D_c , which are the stress drop, the yield stress and the slip weakening distance, respectively, which are associated to the linear slip weakening law proposed by Ida (1972). We computed the fracture energy rate ($G_c = T_\mu D_c / 2$) from the inverted friction law.

Wave propagation from the seismic source to the stations was computed using the AXITRA software (Bouchon, 1981; Coutant, 1990), considering a 1-D velocity model appropriate for the region (Husen et al., 1999). The Neighborhood Algorithm was used to obtain the model that best fits the data (Sambridge, 1999). The misfit (χ^2) between observed and synthetic records for each of the models tested was computed using a normalized L2 norm:

$$\chi^2 = \frac{\sum_i (Obs_i - Synth_i)^2}{\sum_i Obs_i^2} \quad (1)$$

In order to compare the stress drop obtained from the dynamic inversion with other commonly used methodologies, we estimated the stress drop considering a circular crack model of radius r , where the seismic moment (M_0) in terms of the stress drop ($\Delta\sigma$) is given by (Madariaga and Ruiz, 2016)

$$M_0 = \frac{16}{7} \Delta\sigma r^3 \quad (2)$$

The seismic moment was obtained from the magnitude M_w and we estimated the fault radius using the following approximations: (1) average of the semi-axes of the ellipse obtained from the best kinematic and dynamic models, or (2) from a Brune's (1970) far field radiation model considering the observed corner frequency, where the corner frequency (f_c) is given by

$$f_c = k \frac{\beta}{r} \quad (3)$$

Here β is the shear-wave velocity in the vicinity of the source, obtained from the 1D velocity model of Husen et al. (1999). k is a

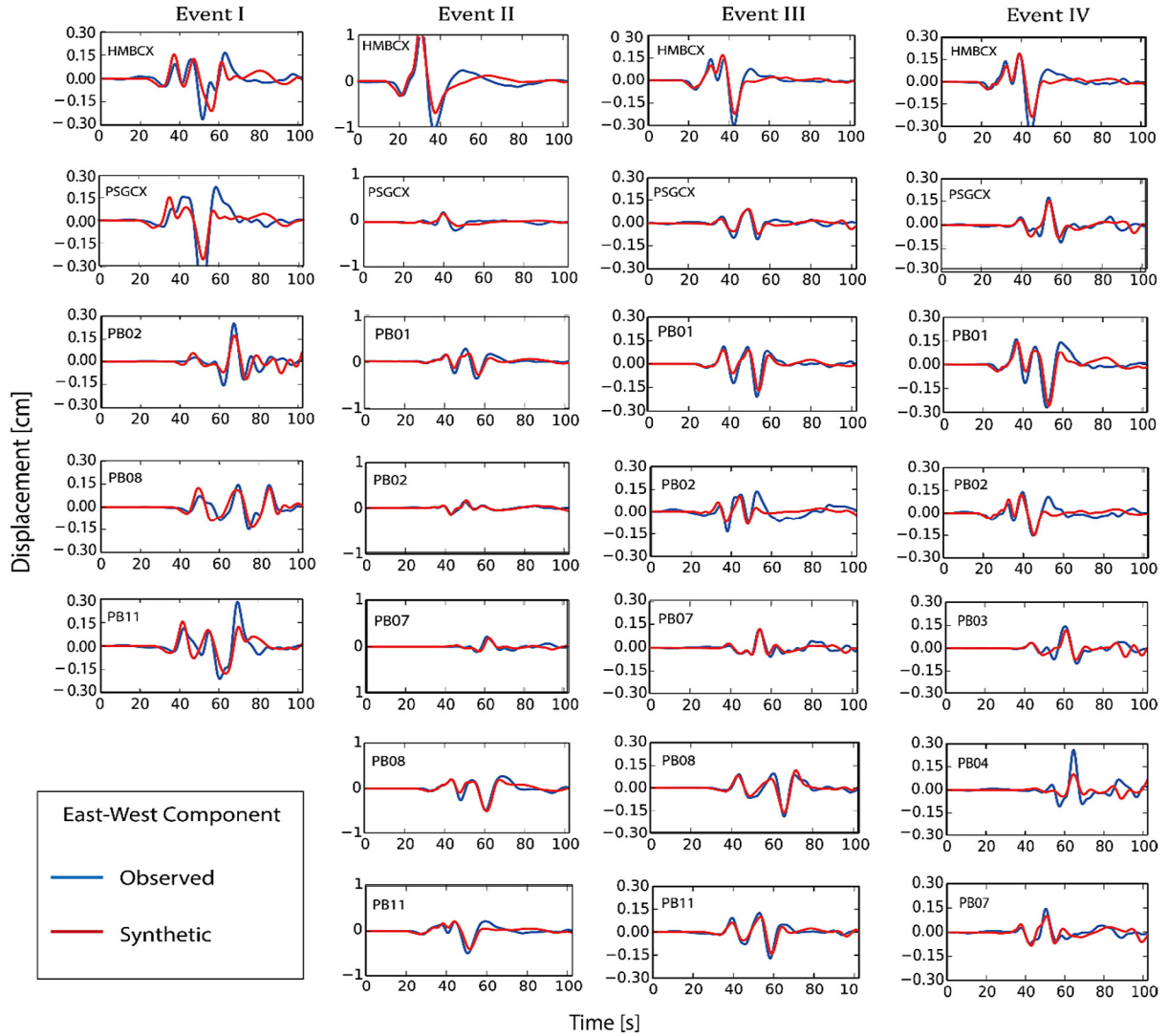


Fig. 3. Comparison between observed and synthetic seismograms on the East-West component, for the best model obtained by dynamic inversion using the Neighborhood Algorithm for the four events studied.

numerical coefficient that Brune (1970) proposed to be 0.372 and Madariaga (1976) proposed $k = 0.21$ using a quasi-dynamic model. Here we will use Brune's coefficient in the computation of fault parameters.

Finally, we compare the dynamic rupture of the events I-IV with five intraplate intermediate-depth earthquakes that occurred in Northern Chile, Japan, Argentina, Mexico, and the Mw 6.9 Valparaiso interplate thrust earthquake. The dynamic rupture of all these events was obtained using a very similar methodology (Ruiz and Madariaga, 2011, 2013; Díaz-Mojica et al., 2014; Herrera et al., 2017; Ruiz et al., 2017; Mirwald et al., 2019).

3. Results

We first carried out kinematic inversions for each of the two nodal planes listed in Table A.1 for each of the earthquakes. Dynamic inversions were then performed using the nodal plane that presented the lowest misfit in the kinematic inversion. In the dynamic inversion we used the geometric parameters of the best kinematic model as a reference to constrain the search interval for the dynamic elliptical patch. We did this since the dynamic inversion is computationally expensive and it can take a long time to converge to a reasonable model. The misfits obtained from the

kinematic inversion for both nodal planes of each of the four events are shown in Table B.1, and in Figs. B.1-2 we show the convergence of kinematic inversion for each fault plane. Rupture planes with the lowest kinematic inversion misfit are those with low dip angles, which agrees with the main subduction interface geometry in Chile. Figures in Appendix B shows the comparison between observed (blue) and best-fit (red) seismograms from the kinematic inversion for the four events studied.

In Fig. 2 we show the slip distribution for the best kinematic model for each of the four earthquakes analyzed considering the nodal plane with lowest misfit. The kinematic source geometry shows that events I-III have a southwest or south orientation for their elliptical patches, while event IV has a northwest orientation. The rupture velocities that were obtained for each of these events were 2.08 km/s, 1.78 km/s, 2.03 km/s and 1.93 km/s, respectively. Values of the moment, M_w and maximum slip are listed at the top left of each slip distribution. The comparison between observed and synthetic seismograms and the convergence of the kinematic parameters together with their uncertainties are shown in Appendix B.

The convergence of the dynamic inversion algorithm for each of the events is shown in Fig. C.1 where we plot the misfit computed for the iterations. The color of the dots is the misfit computed us-

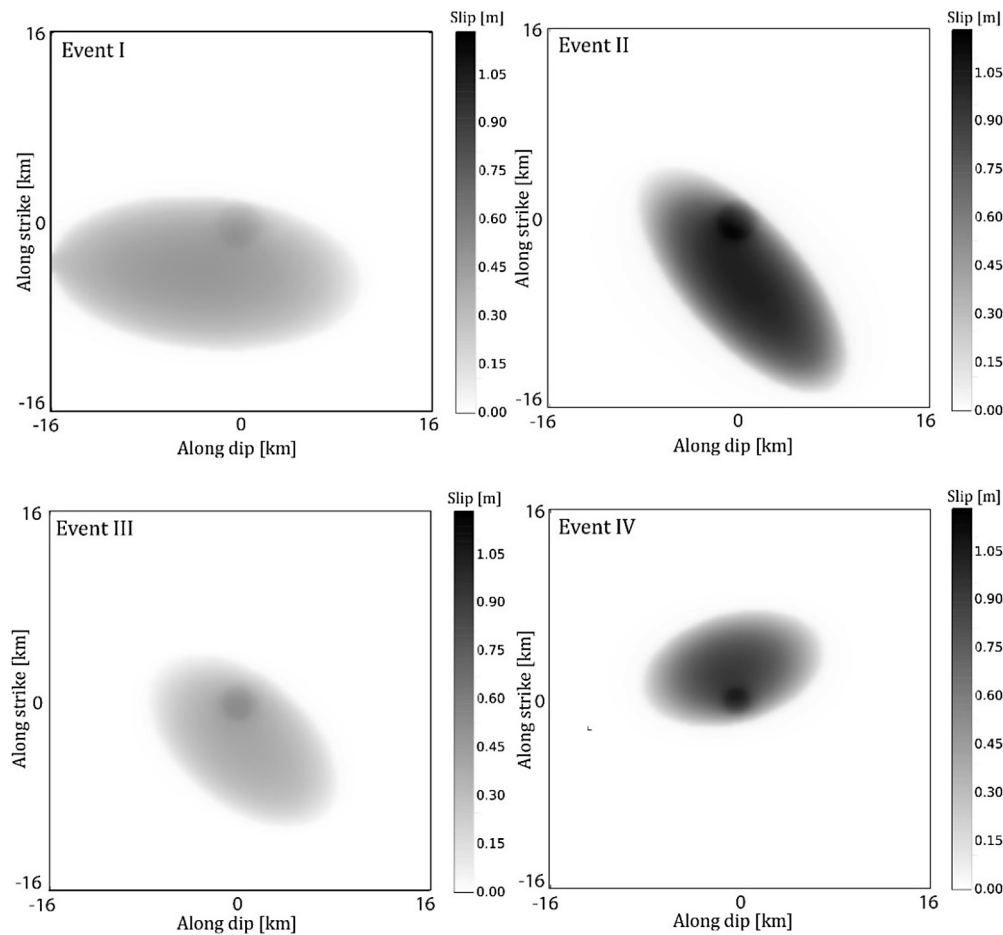


Fig. 4. Dynamic inversion of the four earthquakes. Co-seismic slip distribution of the best dynamic model obtained by the Neighborhood Algorithm for the four earthquakes analyzed in this work.

ing Eq. (1). The inversions converge after 13000 to 23000 iterations with a stable final misfit. The misfit found for earthquakes I-IV were 0.42, 0.21, 0.23 and 0.23, respectively. In Fig. 3, we show the comparison between observed EW seismograms and those computed for the best model obtained from dynamic inversion for the four earthquakes. In Figs. C.14-15 of the supplementary material we show the NW and Up-down components, respectively. It is interesting to note that event II, the largest of the four, had the lowest misfit. This event is the closest to the recording sites (see Fig. 1).

Fig. 4 shows the co-seismic slip distribution for the four events, and Fig. 5 shows slip rate snapshots as a function of time, highlighting the rupture propagation with intervals of 1.0 s for event II and 0.8 s for events I, III and IV. From Figs. 4 and 5 we see that the geometry of the rupture zone for the foreshock I and aftershocks II-III are very well represented by an ellipse, with the centers of the elliptical patches located southwest or south of their respective hypocenters (see Table C.1) and rupture propagating mainly to the southwest or south. The maximum co-seismic slips for these events are 0.51, 1.16 and 0.52 m, respectively (Fig. 4a-c). For aftershock IV, we obtained an elliptical rupture with a propagation to the north from the hypocenter, having a maximum co-seismic slip of 1.03 m (Fig. 4d and 5d). The geometry of the rupture determined from dynamic inversions seems to agree very well with the results of the kinematic inversions shown in Fig. 2, but for the maximum co-seismic slips we found some differences for events I, III and IV (Fig. 2 and 4).

In order to illustrate the convergence of the inversion algorithm, in Appendix C we show the results of each dynamic model developed here. Fig. 6 shows the convergence of different dynamic parameters of event III. Fig. 7 shows the geometry of the rupture computed during different iterations of the inversion process as the misfit approaches the optimal value. We observe that the ellipses close to the best fitting model are very similar. These results could be used to estimate the variance of the inversion as is usually done in Bayesian methods (Galovič et al., 2019).

In Fig. 8 we show the geographic and tectonic context of the four co-seismic models calculated in this work.

Fig. 9 shows a comparison between the dynamic parameters (T_e , T'_μ and G_c) for interplate and intraplate intermediate depth earthquakes for which dynamic inversion results are available (Table C.2). Results are shown on a logarithmic plot of the rupture surface against the seismic moment. The straight lines are the relations expected for circular cracks with constant stress drop (Kanamori and Anderson, 1975). In the same figure we plot results for a number of intermediate depth earthquakes obtained by previous dynamic inversions: VI) Jujuy earthquake 2015, VII) Michilla earthquake 2007, VIII) Iwate earthquake 2008, IX) Zumpango earthquake 2011, X) Mexican earthquake 2017. And we also plot the results of dynamic inversion of the: V) Valparaiso earthquake of 2017 by Ruiz et al. (2017). The four events studied here are all highlighted inside the blue lozenge. It is remarkable that the stress drop varies only between 2.29 and 7.46 MPa, while the stress inside the nucleation zone varies between 3.66 and 11.33 MPa, with a variability of approximately 3-fold in both cases, sug-

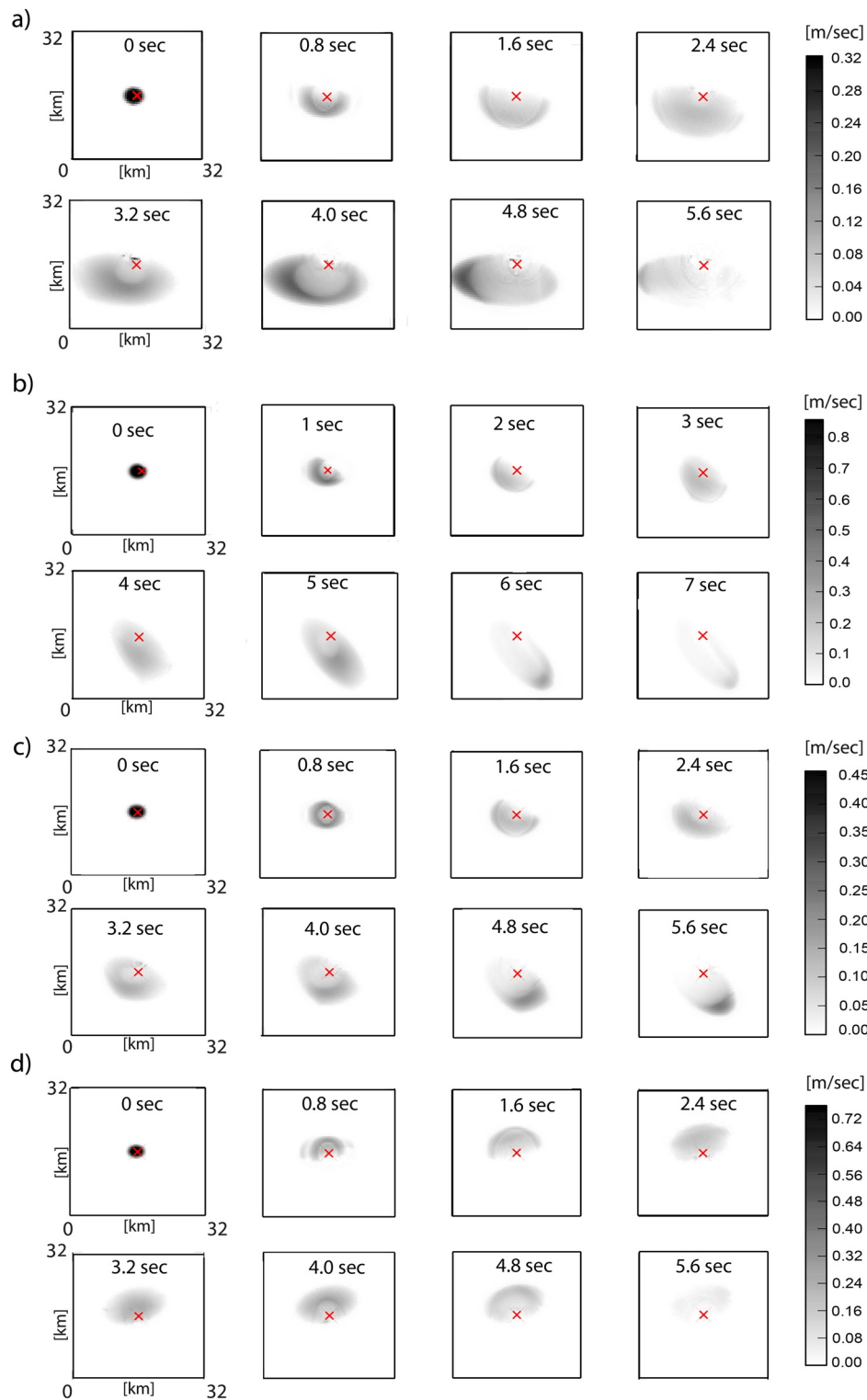


Fig. 5. Snapshots for the slip rate obtained by dynamic inversion of the events studied. (a) Event I, (b) event II, (c) event III and (d) event IV. The time at which the slip rate was computed is indicated at the top of each snapshot. The value of slip rate is indicated with the gray scale plotted at the right of each figure.

gesting a similar uncertainty. The largest variation observed is for the fracture energy release rate which varies almost eight-fold between 0.36 and 3.03 MJ/m². The full set of dynamic parameters determined by inversion is shown in Table C.1 and its uncertainties in Appendix C.

In Fig. 10 we compared the stress drop values obtained using different methodologies for earthquakes I-X.

4. Discussion

We carried out kinematic and dynamic inversions of one foreshock and three aftershocks of the 2014 Iquique earthquake to better understand the rupture process of earthquakes occurring close to the trench and below the continental wedge on the plate interface; specifically, in the transition zone (TZ) proposed by Maksymowicz et al. (2018). It should be remarked that in the inversions

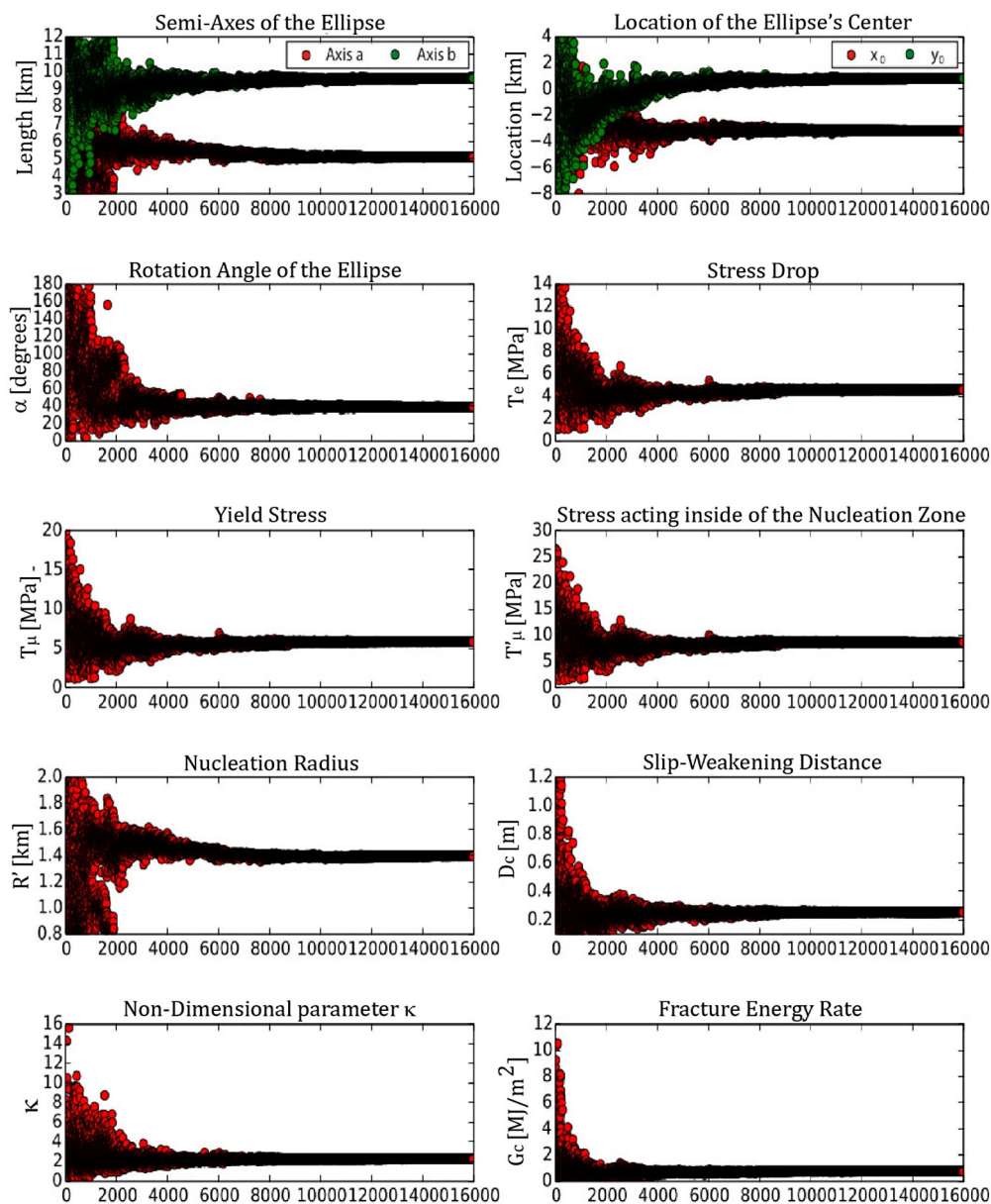


Fig. 6. Convergence of the dynamic parameters as a function of the model number sampled by the Neighborhood Algorithm for event III. The non-dimensional parameter (κ) is defined in Appendix C.

we used the full records filtered in a frequency band that includes the corner frequency, but this frequency band was a bit narrower for event I (from 0.02 to 0.18 Hz), since the inversions were less accurate in a wider frequency band (see Appendix B), because our numerical model does not properly take into account the surface waves that are generated by shallow events. Event I is the closest to the trench and the surface (see Fig. 8), so the waveform fit was not as good as for events II-IV (Fig. 3).

The co-seismic slip model of the mainshock in Fig. 1 indicates that the rupture stopped in the transition zone (TZ) and that the foreshock and aftershock distribution reached the boundary between the TZ and the frontal accretionary prism (FAP), while seismicity was almost absent in the frontal unit. The TZ is rheologically stronger than the unconsolidated and semi-consolidated sediments of the FAP (Byrne et al., 1988; Wells et al., 2003; Moscoso et al., 2011; Maksymowicz et al., 2018). The earthquakes analyzed in this study are located in the TZ or approximately at its border, since the TZ is roughly correlated with the middle continental slope (Maksy-

mowicz et al., 2018), located between the MLS break and the SB line (Fig. 1 and 8a). Then, considering the location of these events, with hypocentral depths varying between 17.8 and 28 km, their reverse focal mechanisms reported by the GCMT and the results of the kinematic inversions for the nodal planes NP1 and NP2 (Table B.1), we infer that the rupture plane of each of these events is located on the plate interface. In fact, as shown in Fig. 8b they fit very well with the geometry of the Slab 1.0 model proposed by Hayes et al. (2012). Also, Fig. 8 shows that the seismic rupture of foreshock I began in the TZ and apparently stopped at the base of the FAP. Furthermore, this figure shows that the rupture zones of aftershocks III-IV are completely inside the TZ, while the rupture zone of aftershock II is at the boundary between the TZ and the dense basement below the CS.

The kinematic and dynamic inversion results show that the geometry of rupture inverted for these events are very similar to each other as could be expected for shallow interplate events. The estimated rupture area, slip distribution, source duration, stress

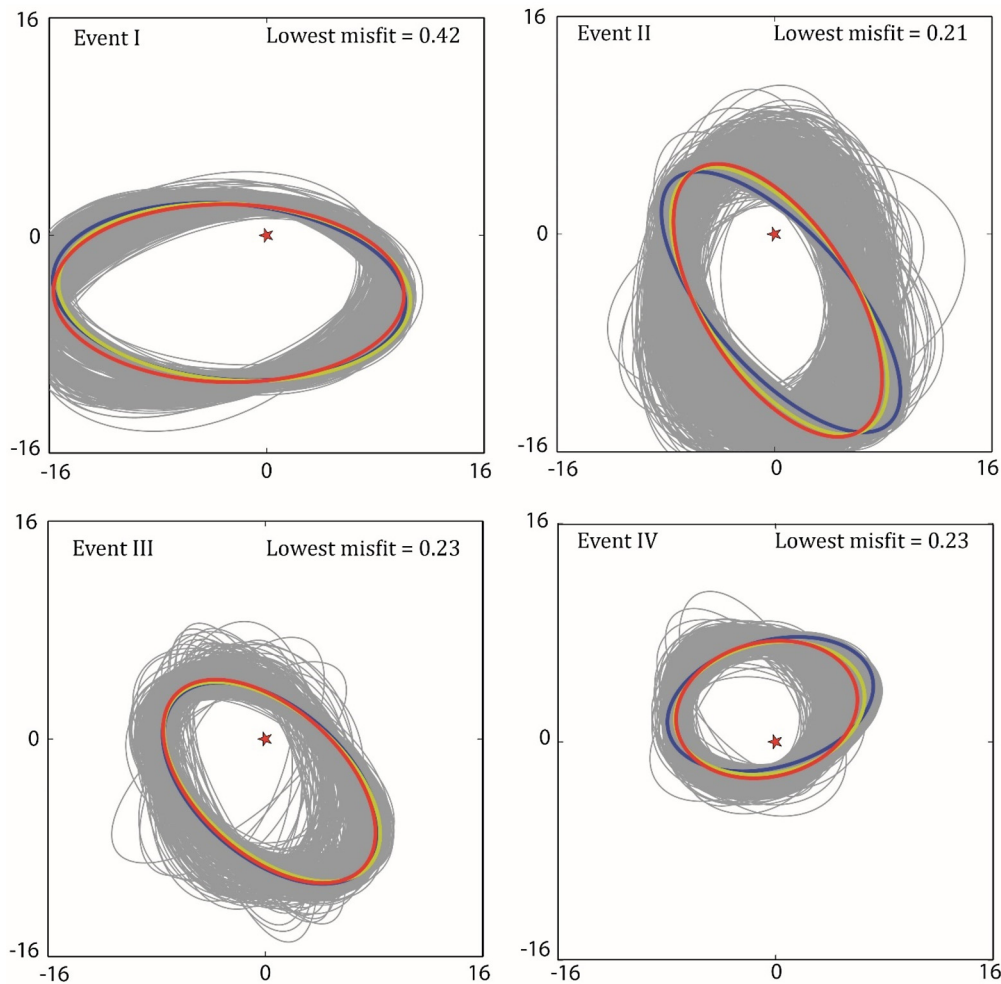


Fig. 7. Convergence of dynamic inversion. In gray, we plot the source ellipses for iterations close to the optimal solution (lowest misfit) for the four inverted events (I-IV). We considered ranges between 90% and 100% of the best fit, where $\text{fit} = 1 - \text{misfit}$. The blue ellipse is the one that has the minimum misfit. The red ellipse corresponds to 95% of the best fit. The yellow ellipse corresponds to the average of all ellipses in the range considered. The red stars denote the hypocenters of the events.

drop and other dynamic parameters of these four events (see Figs. 4–5, 7–9 and Table C.1) seem to be typical of interplate earthquakes around Mw 6.5 when we compare our results with published scaling laws and empirical relations (Molnar and Wyss, 1972; Sykes and Sbar, 1973; Kanamori and Anderson, 1975). To further confirm this idea, we show in Fig. 9 the relation between fault surface area (S) and seismic moment (M_0) for the four earthquakes analyzed in this study, together with the 2017 Mw 6.9 Valparaíso interplate earthquake (Ruiz et al., 2017), and five intraplate intermediate-depth earthquakes (Ruiz and Madariaga, 2011, 2013; Díaz-Mojica et al., 2014; Herrera et al., 2017; Mirwald et al., 2019), which were dynamically modeled using a very similar methodology. The four events studied in this work are in the zone defined for interplate earthquakes by Kanamori and Anderson (1975) from empirical evidence (see blue lozenge in Fig. 9), although there could be some degree of inaccuracy due to the different methodologies and estimates used. In Fig. 10 we observe that the stress drops obtained using a Brune's (1970) source model with a fault radius derived from the observed corner frequency (blue bar), are less than those obtained using a more complete dynamic model (red bar) for events II-IV, which seems to agree with what was proposed by Gallovič and Valentová (2020). For event I, on the other hand, the estimated stress drop using a Brune's source model is greater than that obtained from dynamic inversion. We think that the differences observed between the red and blue bars in Fig. 10 for the events studied can be explained by the differences between

simplified and a more complete dynamic model. For the simple dynamic model, we assume a circular instantaneous rupture model that produces only S waves (Brune, 1970). For the dynamic model, instead, we consider a more complete seismic rupture process and the complete radiated field. On the other hand, when we used the source size obtained from the kinematic (brown bar) and dynamic (orange bar) inversions to estimate the stress drop, we observe a very good agreement with the stress drop from dynamic models, which agrees with what was observed by Gallovič and Valentová (2020). In supplementary material we add estimates for the corner frequency of the interplate earthquakes studied here, using Eq. (3), and considering the semi-axes average of the ellipse obtained from the best kinematic and dynamic models as fault radius (see Tables D.1-2). We found a very reasonable agreement between the observed corner frequency and the estimated corner frequency using the source size derived from the inversions, especially when we used the dynamic model, which was also observed by Gallovič and Valentová (2020) analyzing synthetic dynamic rupture models.

We observe that some inverted dynamic parameters appear to be different from those of intraplate intermediate depth earthquakes, particularly the stress drop, the yield stress, the stress acting inside of the nucleation zone and the fracture energy rate (see Tables C.1 and C.2). In particular, Fig. 9a shows that the stress drop of interplate earthquakes is generally smaller than the stress drop of intraplate intermediate depth earthquakes, which is in agreement with previous observations (Molnar and Wyss, 1972; Sykes

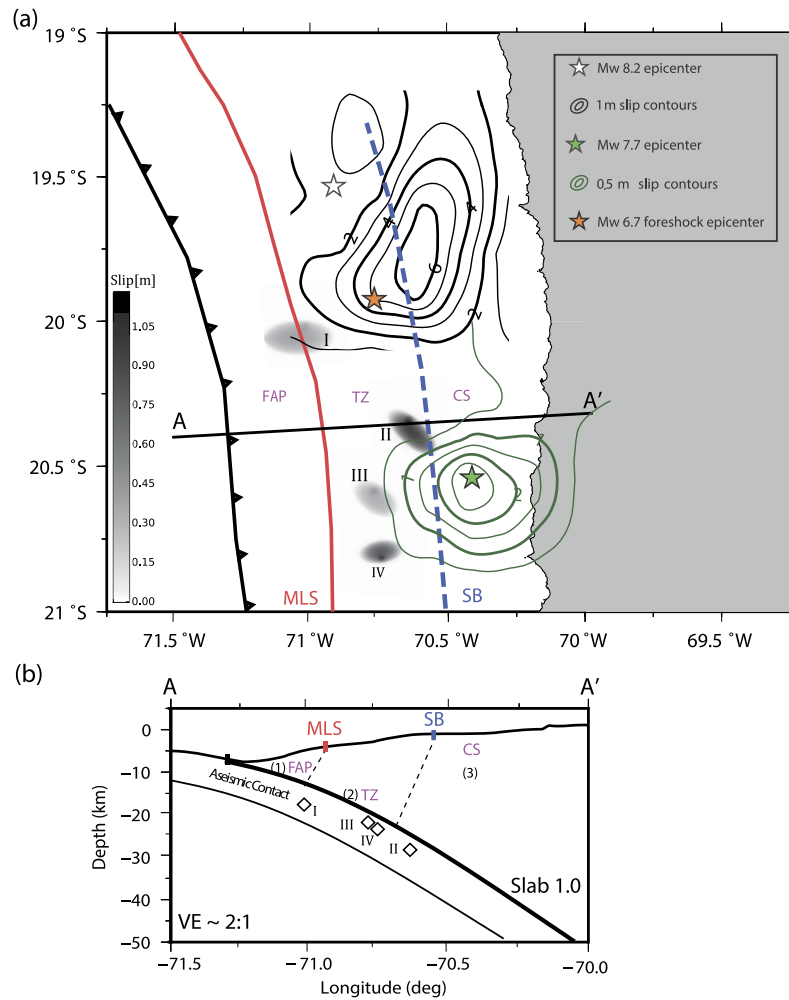


Fig. 8. (a) Co-seismic slip distribution in the study area. The dynamic co-seismic models of the events considered in this work are shown in gray. The co-seismic ruptures of the Mw 8.2 mainshock and its Mw 7.7 aftershock are shown with contours. The red line indicates the limit between the lower and middle slopes (MLS) and the dotted blue line indicates the shelf-break (SB). (b) Cross section AA', which shows with diamonds the hypocenters of the earthquakes analyzed in this study. The dotted lines correspond to an estimate of the separation between the three main units of the continental wedge proposed by Maksymowicz et al. (2018): (1) frontal accretionary prism (FAP), (2) transition zone (TZ) in the plate interface and (3) a dense basement below the continental shelf (CS). The subduction interface is plotted using the Slab 1.0 model (Hayes et al., 2012).

and Sbar, 1973; Kanamori and Anderson, 1975; Leyton et al., 2009), but this time all these events were analyzed considering a more complete dynamic model.

Fig. 9b shows that the values of the stress acting inside of the nucleation zone seems to accentuate the difference between the two types of earthquakes, reaching very high values for intraplate intermediate depth earthquakes compared to interplate events. This is agreement with the fracture energy rate (G_c), which tends to be lower for interplate earthquakes compared with intraplate intermediate depth events (Fig. 9c). This result could reflect the significant differences in rheology and tectonic stresses to which these two types of earthquakes are subjected.

Figs. 4, 5 and 8 show that events I-III have a seismic rupture propagating mainly to the southwest (towards the trench) or south. Conversely, event IV shows a propagation towards the north, northwest and northeast. In all cases the seismic rupture seems to show no difficulty to propagate towards the FAP on the plate interface, especially for event I, which apparently has propagated from the TZ to the base of the FAP (Fig. 8). The large values of the slip rate are concentrated in the nucleation zone and along the rupture front, being smaller in latter stages, probably because the acceleration and deceleration of the rupture are not very high, which seems to be in agreement with the low rupture velocities found

in kinematic inversions, which vary between 1.78 and 2.08 km/s. On the other hand, the maximum slip varying between 0.49 and 1.16 m seems normal for this type of earthquakes (Fig. 4). Furthermore, the maximum slip of 1.16 m obtained for event II from the dynamic inversion is very similar to that obtained from the kinematic inversion (Fig. 2), and although there are some discrepancies for the other events, we think that these differences could be just a consequence of using different approximations to the seismic source.

The event I located closer to the trench in the TZ has lower stress drop (T_e), yield stress (T_μ), stress acting inside of a circular nucleation (T'_μ), slip weakening distance (D_c), fracture energy rate (G_c) and total fracture energy (G_t) values than the other three interplate events studied in this work (see Table C.1). We think that despite the increase in presence of fluids, porosity and the fracturing of rock towards the trench, these differences could be in part a consequence of the change in tectonic stresses along the TZ after the 2014 Mw 8.2 Iquique earthquake occurred, since event I was a foreshock and events II-IV were aftershocks of the main-shock, having these four events similar magnitude.

Comparing the four events studied with event V, the Mw 6.9 Valparaiso interplate earthquake (Ruiz et al., 2017), we observe that the latter event has slightly higher T_e , T_μ and T'_μ values,

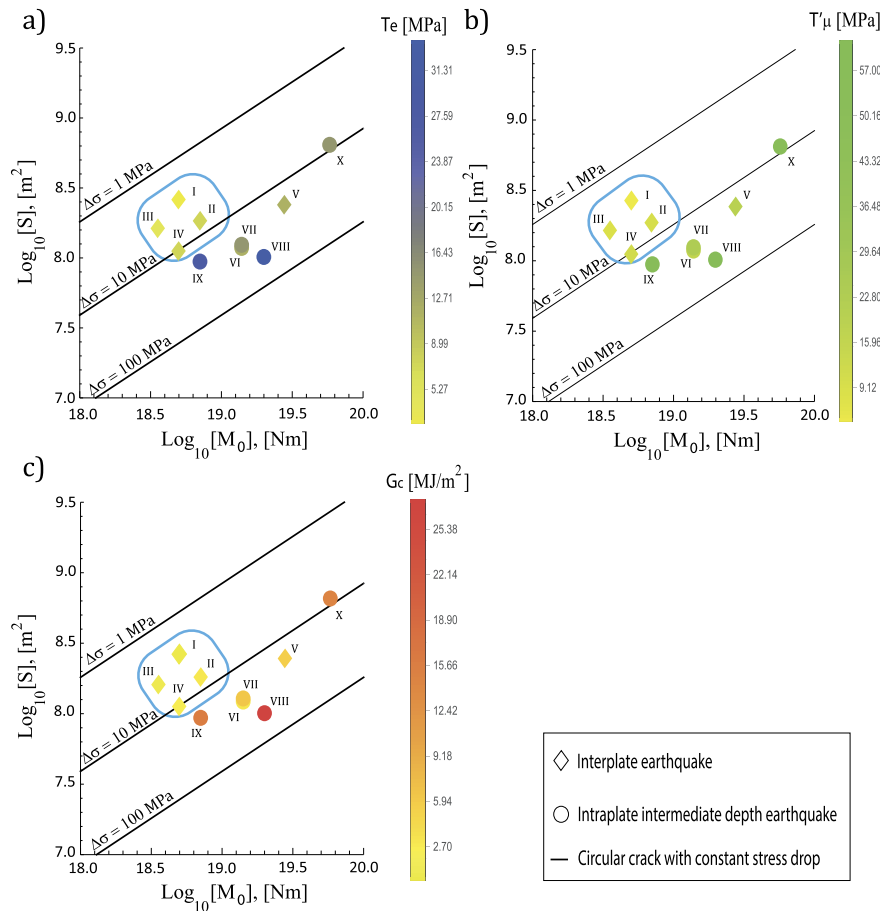


Fig. 9. Relation between fault surface area (S) and seismic moment (M_0). In (a) stress drop of the events is compared, in (b) stress in the nucleation zone is compared, and in (c) fracture energy release rate is compared. The four interplate earthquakes studied in this work (events I–IV) are enclosed by the blue lozenge. Event V is the Mw 6.9 Valparaiso earthquake (Ruiz et al., 2017). Events VI–X are previously studied intraplate intermediate depth earthquakes (Herrera et al., 2017; Ruiz and Madariaga, 2011, 2013; Díaz-Mojica et al., 2014; Mirwald et al., 2019).

which is consistent with the fact that this event occurred about 100 km landward from trench. Therefore, since event I occurred near the up-dip limit (unit (2) Fig. 8b), event III occurred approximately in the middle of the TZ (unit (2) Fig. 8b), and events IV and II occurred in unit (2) and its border (Fig. 8b), we infer that the TZ is suitable for the nucleation of small and moderate magnitude (up to $M_w \sim 6$), and that this zone does not seem to be a barrier for the propagation of seismic ruptures to the boundary between the TZ and the FAP.

The 2014 Iquique earthquake occurred in a recognized seismic gap that according to Métois et al. (2016) had an estimated seismic moment deficit corresponding to a magnitude of $M_w \sim 8.6$. The 2014 Iquique earthquake was an $M_w 8.2$ event and its biggest foreshock and aftershock were $M_w 6.7$ and 7.7 , respectively. We consider that there is still enough accumulated energy in northern Chile to produce earthquakes of magnitude $M_w > 8.0$ in the future. In addition, taking into account the results of this study, we propose that the TZ in the studied area shows no impediment for the seismic rupture of large interplate earthquakes to propagate towards the limit between the TZ and the FAP, a potential tsunamigenic zone. We think that this up-dip limit should control the transition between stable sliding (aseismic) and unstable stick-slip frictional sliding (seismogenic) (Byrne et al., 1988; Moscoso et al., 2011), since it is known that the stable sliding between the plates is facilitated by the presence of over pressured and unconsolidated sediments at the frontal unit, which is characterized by the absence of both strong and weak thrust earthquakes (Byrne et al., 1988; Moscoso et al., 2011). In summary, we estimate that even

larger tsunamis than that of the 2014 Mw 8.2 Iquique earthquake (An et al., 2014) could occur if an interplate earthquake of similar magnitude reaches the up-dip limit, especially in the latitudes of northern Chile where the frontal accretionary prism is narrow. It is also possible that a giant earthquake ($M_w \sim 9$) could move the FAP by stable aseismic sliding and/or an anelastic deformation in the accretionary prism, as proposed by Scholz (2002), and/or by means of elastic deformation inside of the FAP, as proposed by Wang and Hu (2006). The latter authors consider that the outer wedge is not perfectly plastic and is capable of storing elastic strain energy in its stable regime. Therefore, in the case that a giant earthquake, like the 1877 event (Fig. 1), we propose that it could produce a very large tsunami, as it happened with the 2010 Mw 8.8 Maule earthquake (Maksymowicz et al., 2017; Contreras-Reyes et al., 2017). In particular, Maksymowicz et al. (2017) showed that the co-seismic slip of the Maule earthquake extended up to 6 km landwards from the axis of the trench (deformation front), implying that the slip must have propagated along the entire base of the middle prism, which would correspond to the TZ for the Iquique region.

5. Conclusions

The geometry of the seismic rupture obtained from the kinematic and dynamic inversions are similar for the four earthquakes studied in this work. The dynamic source parameters of these events show that they are actually very similar to each other, corresponding to typical interplate thrust earthquakes around $M_w 6.5$, where their values of stress inside of the nucleation zone, the

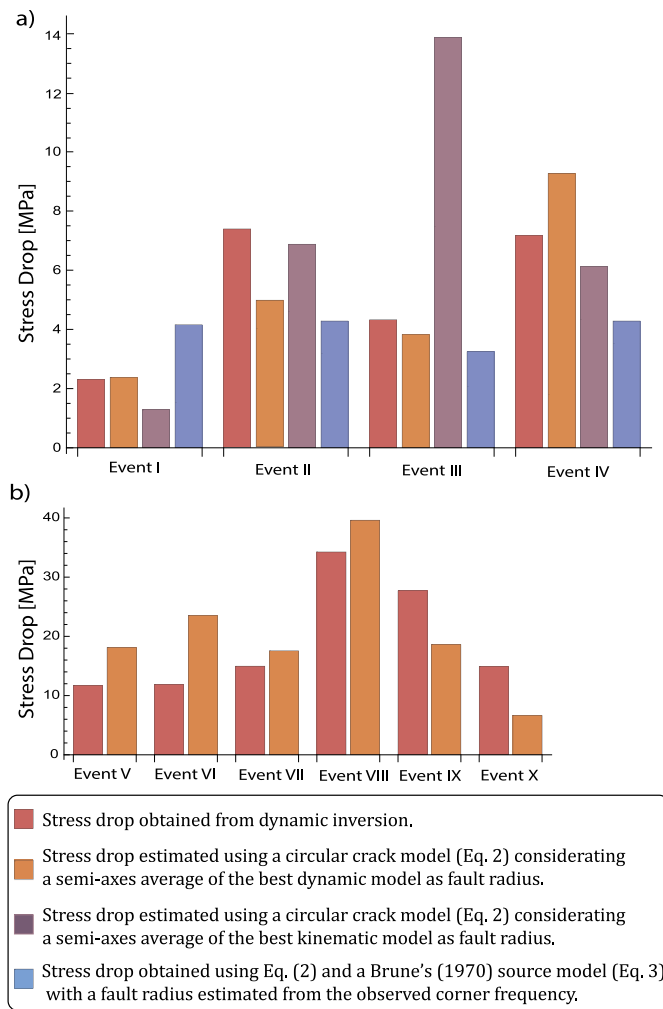


Fig. 10. Comparison between the stress drop obtained from dynamic inversion with some methods used to estimate the stress drop. (a) earthquakes studied in this work (I-IV), (b) previously studied earthquakes (V-X).

stress drop and the fracture energy rate tend to be lower than those of intermediate depth events. This trend is consistent with previous observations of the stress drop, but more observations from full dynamic inversions may be necessary to infer a general trend of some dynamic parameters as those presented here. We also conclude that the different methodologies used seem to provide good estimators of the values of stress drop, fault radius and corner frequency at least for small to moderate magnitude earthquakes, even if some differences are found, that can obviously be explained by the use of a simple and a more complete dynamic model.

Finally, we infer that the Transition Zone in the studied area is suitable for earthquake nucleation of small to moderate magnitude earthquakes, and that it does not behave as a seismic barrier unlike the FAP, allowing the propagation of tsunamigenic earthquakes, especially where the FAP is narrower in northern Chile.

CRedit authorship contribution statement

Cristian Otarola: Conceptualization, Data curation, Formal analysis, Investigation, Methodology, Visualization, Writing – original draft, Writing – review & editing. **Sergio Ruiz:** Conceptualization, Funding acquisition, Resources, Supervision, Validation, Writing – review & editing. **Carlos Herrera:** Formal analysis, Software, Validation, Writing – review & editing. **Raúl Madariaga:** Formal analysis,

Software, Validation, Writing – review & editing. **Cristián Siegel:** Data curation, Validation, Writing – review & editing.

Declaration of competing interest

The authors declare that they have no known competing financial interests or personal relationships that could have appeared to influence the work reported in this paper.

Acknowledgements

This research was funded by Fondecyt contract Numbers 1170430 and 1200779. We acknowledge support by program PRS (Programa de Riesgo Sísmico) of the University de Chile. Seismic waveform data were obtained from the network Centro Sismológico Nacional (www.sismologia.cl) and IPOC network (<https://doi.org/10.14470/PK615318>). Maps were created using Generic Mapping Tools version 5.4.5. We also thank František Gallovič and an anonymous reviewer for their very thoughtful and constructive comments.

Appendix A. Supplementary material

Supplementary material related to this article can be found online at <https://doi.org/10.1016/j.epsl.2021.116842>.

References

- An, C., Sepulveda, I., Liu, P.L.-F., 2014. Tsunami source and its validation of the 2014 Iquique, Chile earthquake. *Geophys. Res. Lett.* 41, 3988–3994. <https://doi.org/10.1002/2014GL060567>.
- Bouchon, M., 1981. A simple method to calculate Green's functions for elastic layered media. *Bull. Seismol. Soc. Am.* 71 (4), 959–971.
- Byrne, D.E., Davis, D.M., Sykes, L.R., 1988. Loci and maximum size of thrust earthquakes and the mechanics of the shallow region of subduction zones. *Tectonics* 7 (4), 833–857. <https://doi.org/10.1029/TTC007i004p00833>.
- Brune, J.N., 1970. Tectonic stress and the spectra of seismic shear waves from earthquakes. *J. Geophys. Res.* 75, 4997–5009. <https://doi.org/10.1029/JB075i026p04997>.
- Cesca, S., Grigoli, F., Heimann, S., Dahm, T., Kriegerowski, M., Sobiesiak, M., Tassara, C., Olcay, M., 2016. The M_w 8.1 2014 Iquique, Chile, seismic sequence: a tale of foreshocks and aftershocks. *Geophys. J. Int.* 204 (3), 1766–1780. <https://doi.org/10.1093/gji/ggv544>.
- Contreras-Reyes, E., Jara, J., Grevemeyer, I., et al., 2012. Abrupt change in the dip of the subducting plate beneath North Chile. *Nat. Geosci.* 5, 342–345. <https://doi.org/10.1038/ngeo1447>.
- Contreras-Reyes, E., Maksymowicz, A., Lange, D., Grevemeyer, I., Muñoz-Linford, P., Moscoso, E., 2017. On the relationship between structure, morphology and large coseismic slip: a case study of the M_w 8.8 Maule, Chile 2010 earthquake. *Earth Planet. Sci. Lett.* 478, 27–39. <https://doi.org/10.1016/j.epsl.2017.08.028>.
- Coutant, O., 1990. Programme de Simulation Numérique AXITRA, Rapport LGIT. Université Joseph Fourier, Grenoble, France.
- Di Carli, S., Francois-Holden, C., Peyrat, S., Madariaga, R., 2010. Dynamic inversion of the 2000 Tottori earthquake based on elliptical subfault approximations. *J. Geophys. Res.* 115 (B12). <https://doi.org/10.1029/2009JB006358>.
- Díaz-Mojica, J., Cruz-Atienza, V.M., Madariaga, R., Singh, S.K., Tago, J., Iglesias, A., 2014. Dynamic source inversion of the $M_{6.5}$ intermediate-depth Zumpango earthquake in central Mexico: a parallel genetic algorithm. *J. Geophys. Res.* 119, 7768–7785. <https://doi.org/10.1002/2013JB008854>.
- Duputel, Z., Jiang, J., Jolivet, R., Simons, M., Rivera, L., Ampuero, J.-P., Riel, B., Owen, S.E., Moore, A.W., Samsonov, S.V., et al., 2015. The Iquique earthquake sequence of April 2014: Bayesian modeling accounting for prediction uncertainty. *Geophys. Res. Lett.* 42, 7949–7957. <https://doi.org/10.1002/2015GL065402>.
- Gallovič, F., Valentová, L., Ampuero, J.-P., Gabriel, A.-A., 2019. Bayesian dynamic finite-fault inversion: 1. Method and synthetic test. *J. Geophys. Res., Solid Earth* 124, 6949–6969. <https://doi.org/10.1029/2019JB017510>.
- Gallovič, F., Valentová, L., 2020. Earthquake stress drops from dynamic rupture simulations constrained by observed ground motions. *Geophys. Res. Lett.* 47, e2019GL085880. <https://doi.org/10.1029/2019GL085880>.
- Geersen, J., Ranero, C.R., Kopp, H., Behrmann, J.H., Lange, D., Klauke, I., Barrientos, S., Diaz-Naveas, J., Barckhausen, U., Reichert, C., 2018. Does permanent extensional deformation in lower forearc slopes indicate shallow plate-boundary rupture? *Earth Planet. Sci. Lett.* (ISSN 0012-821X) 489, 17–27. <https://doi.org/10.1016/j.epsl.2018.02.030>.

- González, G., Salazar, P., Loveless, J.P., Allmendinger, R.W., Aron, F., Shrivastava, M., 2015. Upper plate reverse fault reactivation and the unclamping of the megathrust during the 2014 northern Chile earthquake sequence. *Geology* 43 (8), 671–674. <https://doi.org/10.1130/G36703.1>.
- Hayes, G.P., Wald, D.J., Johnson, R.L., 2012. Slab1.0: a three-dimensional model of global subduction zone geometries. *J. Geophys. Res.* 117, B01302. <https://doi.org/10.1029/2011JB008524>.
- Herrera, C., Ruiz, S., Madariaga, R., Poli, P., 2017. Dynamic inversion of the 2015 Jujuy earthquake and similarity with other intraslab events. *Geophys. J. Int.* 209 (2), 866–875. <https://doi.org/10.1093/gji/ggx056>.
- Husen, S., Kissling, E., Flueh, E., Asch, G., 1999. Accurate hypocentre determination in the seismogenic zone of the subducting nazca plate in northern Chile using a combined on-/offshore network. *Geophys. J. Int.* 138 (3), 687–701. <https://doi.org/10.1046/j.1365-246x.1999.00893.x>.
- Ida, Y., 1972. Cohesive force across the tip of a longitudinal-shear crack and Griffith's specific surface energy. *J. Geophys. Res.* 77 (20), 3796–3805. <https://doi.org/10.1029/JB077i020p03796>.
- Kanamori, H., Anderson, D.L., 1975. Theoretical basis of some empirical relations in seismology. *Bull. Seismol. Soc. Am.* 65 (5), 1073–1095.
- Kato, A., Fukuda, J., Kumazawa, T., et al., 2016. Accelerated nucleation of the 2014 Iquique, Chile Mw 8.2 earthquake. *Sci. Rep.* 6, 24792. <https://doi.org/10.1038/srep24792>.
- Lay, T., Yue, H., Brodsky, E.E., An, C., 2014. The 1 April 2014 Iquique, Chile, Mw 8.1 earthquake rupture sequence. *Geophys. Res. Lett.* 41, 3818–3825. <https://doi.org/10.1002/2014GL060238>.
- León-Ríos, S., Ruiz, S., Maksymowicz, A., Leyton, F., Fuenzalida, A., Madariaga, R., 2016. Diversity of the Iquique's foreshocks and aftershocks: a clue about complex rupture process of a Mw 8.1 earthquake. *J. Seismol.* 20, 1059–1073. <https://doi.org/10.1007/s10950-016-9568-6>.
- Leyton, F., Ruiz, J., Campos, J., Kausel, E., 2009. Intraplate and interplate earthquakes in Chilean subduction zone: a theoretical and observational comparison. *Phys. Earth Planet. Inter.* 175 (1–2), 37–46. <https://doi.org/10.1016/j.pepi.2008.03.017>.
- Leyton, F., Pasten, C., Ruiz, S., Idini, B., Rojas, F., 2018a. Empirical site classification of the CSN network using strong-motion records. *Seismol. Res. Lett.* 89 (2A), 512–518. <https://doi.org/10.1785/0220170167>.
- Leyton, F., Leopold, A., Hurtado, G., Pasten, C., Ruiz, S., Montalva, G., Saez, E., 2018b. Geophysical characterization of the Chilean seismological stations: first results. *Seismol. Res. Lett.* 89 (2A), 519–525. <https://doi.org/10.1785/0220170156>.
- Lomax, A., Virieux, J., Volant, P., Berge-Thierry, C., 2000. Probabilistic earthquake location in 3D and layered models. In: Thurber, C.H., Rabinowitz, N. (Eds.), *Advances in Seismic Event Location*. Springer, pp. 101–134.
- Madariaga, R., 1976. Dynamics of an expanding circular fault. *Bull. Seismol. Soc. Am.* 65, 163–182.
- Madariaga, R., Ruiz, S., 2016. Earthquake dynamics on circular faults: a review 1970–2015. *J. Seismol.* 20, 1235–1252. <https://doi.org/10.1007/s10950-016-9590-8>.
- Maksymowicz, A., Chadwell, D., Ruiz, J., Tréhu, A., Contreras-Reyes, E., Weinrebe, W., Díaz-Naveas, J., Gibson, J.C., Lonsdale, P., Tryon, M.D., 2017. Coseismic seafloor deformation in trench region during the Maule Mw8.8 megathrust earthquake. *Sci. Rep.* 7, 45918. <https://doi.org/10.1038/srep45918>.
- Maksymowicz, A., Ruiz, J., Vera, E., Contreras-Reyes, E., Ruiz, S., Arriagada, C., Bonvalot, S., Bascañan, S., 2018. Heterogeneous structure of the Northern Chile marine fore-arc and its relation to the rupture of the 2014 Mw 8.2 Iquique earthquake and the currents seismic gaps. *Geophys. J. Int.* 215 (2), 1080–1097. <https://doi.org/10.1093/gji/ggy325>.
- Métois, M., Vigny, C., Socquet, A., 2016. Interseismic coupling megathrust earthquakes and seismic swarms along the Chilean subduction zone (38°–18°S). *Pure Appl. Geophys.* 173, 1431–1449. <https://doi.org/10.1007/s00024-016-1280-5>.
- Mirwald, A., Cruz-Atienza, V.M., Díaz-Mojica, J., Iglesias, A., Singh, S.K., Villafuerte, C., Tago, J., 2019. The September 19, 2017 (Mw7.1), intermediate-depth Mexican earthquake: a slow and energetically inefficient deadly shock. *Geophys. Res. Lett.* 46. <https://doi.org/10.1029/2018GL080904>.
- Molnar, P., Wyss, M., 1972. Moments, source dimensions and stress drops of shallow-focus earthquakes in the Tonga-Kermadec arc. *Phys. Earth Planet. Inter.* 6, 263–278. [https://doi.org/10.1016/0031-9201\(72\)90010-6](https://doi.org/10.1016/0031-9201(72)90010-6).
- Moscoso, E., Grevemeyer, I., Contreras-Reyes, E., Flueh, E.R., Dzierma, Y., Rabbel, W., Thorwart, M., 2011. Revealing the deep structure and rupture plane of the 2010 Maule, Chile earthquake (Mw = 8.8) using wide angle seismic data. *Earth Planet. Sci. Lett.* 307, 147–155. <https://doi.org/10.1016/j.epsl.2011.04.025>.
- Ruiz, J., Maksymowicz, A., Ortega-Culaciati, F., Rivera, L., Comte, D., 2019. Source characteristics of the March 16, 2014 Mw 6.7 earthquake and its implications for the Mw 8.2 Pisagua mainshock. *Tectonophysics* (ISSN 0040-1951) 767, 228170. <https://doi.org/10.1016/j.tecto.2019.228170>.
- Ruiz, S., Madariaga, R., 2011. Determination of the friction law parameters of the Mw 6.7 Michilla earthquake in northern Chile by dynamic inversion. *Geophys. Res. Lett.* 38, L09317. <https://doi.org/10.1029/2011GL047147>.
- Ruiz, S., Madariaga, R., 2013. Kinematic and dynamic inversion of the 2008 northern Iwate earthquake. *Bull. Seismol. Soc. Am.* 103 (2A), 694–708. <https://doi.org/10.1785/010120056>.
- Ruiz, S., Métois, M., Fuenzalida, A., Ruiz, J., Leyton, F., Grandin, R., Vigny, C., Madariaga, R., Campos, J., 2014. Intense foreshocks and a slow slip event preceded the 2014 Iquique Mw 8.1 earthquake. *Science* 345, 1165–1169. <https://doi.org/10.1126/science.1256074>.
- Ruiz, S., Aden-Antoniow, F., Baez, J.C., Otarola, C., Potin, B., del Campo, F., Poli, P., Flores, C., Satriano, C., Leyton, F., Madariaga, R., Bernard, P., 2017. Nucleation phase and dynamic inversion of the Mw 6.9 Valparaíso 2017 earthquake in Central Chile. *Geophys. Res. Lett.* 44 (20), 10,290–10,297. <https://doi.org/10.1002/2017GL075675>.
- Ruiz, S., Madariaga, R., 2018. Historical and recent large megathrust earthquakes in Chile. *Tectonophysics* 733, 37–56. <https://doi.org/10.1016/j.tecto.2018.01.015>.
- Sambridge, M., 1999. Geophysical inversion with a neighbourhood algorithm—I. Searching a parameter space. *Geophys. J. Int.* 138 (2), 479–494. <https://doi.org/10.1046/j.1365-246x.1999.00876.x>.
- Scholz, C.H., 2002. *The Mechanics of Earthquakes and Faulting*, 2nd edn. Cambridge Univ. Press, Cambridge.
- Schurr, B., Asch, G., Hainzl, S., et al., 2014. Gradual unlocking of plate boundary controlled initiation of the 2014 Iquique earthquake. *Nature* 512, 299–302. <https://doi.org/10.1038/nature13681>.
- Sykes, L., Sbar, M., 1973. Intraplate earthquakes, lithospheric stresses and the driving mechanism of plate tectonics. *Nature* 245, 298–302. <https://doi.org/10.1038/245298a0>.
- Socquet, A., Valdes, J.P., Jara, J., Cotton, F., Walpersdorf, A., Cotte, N., Specht, S., Ortega-Culaciati, F., Carrizo, D., Norabuena, E., 2017. An 8 month slow slip event triggers progressive nucleation of the 2014 Chile megathrust. *Geophys. Res. Lett.* 44, 4046–4053. <https://doi.org/10.1002/2017GL073023>.
- Soto, H., Sippl, C., Schurr, B., Kummerow, J., Asch, G., Tilmann, F., Comte, D., Ruiz, S., Oncken, O., 2019. Probing the northern Chile megathrust with seismicity - the 2014 Mw 8.1 Iquique earthquake sequence. *J. Geophys. Res., Solid Earth* 124 (12), 12935–12954. <https://doi.org/10.1029/2019JB017794>.
- Vallée, M., Bouchon, M., 2004. Imaging coseismic rupture in far field by slip patches. *Geophys. J. Int.* 156 (3), 615–630. <https://doi.org/10.1111/j.1365-246X.2004.02158.x>.
- Wang, K., Hu, Y., 2006. Accretionary prisms in subduction earthquake cycles: the theory of dynamic Coulomb wedge. *J. Geophys. Res.* 111, B06410. <https://doi.org/10.1029/2005JB004094>.
- Wells, R.E., Blakely, R.J., Sugiyama, Y., Scholl, D.W., Dinterman, P.A., 2003. Basin-centered asperities in great subduction zone earthquakes: a link between slip, subsidence, and subduction erosion? *J. Geophys. Res.* 108 (B10), 250. <https://doi.org/10.1029/2002JB002072>.